# OrbTouch: Recognizing Human Touch in Deformable Interfaces with Deep Neural Networks

Chris Larson \*
Cornell University
Dept. of Mechanical
Engineering
Ithaca, NY 14853
cl966@cornell.edu

Josef Spjut NVIDIA Research NVIDIA Corporation Santa Clara, CA 95050 jspjut@nvidia.com Ross Knepper Cornell University Dept. of Computer Science Ithaca, NY 14853 rak@cs.cornell.edu Rob Shepherd Cornell University Dept. of Mechanical Engineering Ithaca, NY 14853 rfs247@cornell.edu

## **ABSTRACT**

User interfaces provide an interactive window between physical and virtual environments. A new concept in the field of human-computer interaction is a soft user interface; a compliant surface that facilitates touch interaction through deformation. Despite the potential of these interfaces, they currently lack a signal processing framework that can efficiently extract information from their deformation. Here we present OrbTouch, a device that uses statistical learning algorithms, based on convolutional neural networks, to map deformations from human touch to categorical labels (i.e., gestures) and touch location using stretchable capacitor signals as inputs. We demonstrate this approach by using the device to control the popular game Tetris. OrbTouch provides a modular, robust framework to interpret deformation in soft media, laying a foundation for new modes of human computer interaction through shape changing solids.

# **Keywords**

human computer interaction, stretchable electronics, soft robotics, deep learning, information entropy

## Introduction

The use of compliant touch interfaces is a topic of interest within the fields of human computer interaction (HCI) [1] and virtual reality (VR) [2]. Rubber-like materials that deform under the force of human touch potentially combine the gesture capabilities of capacitive touchscreens [3] with the tactile feedback of physical buttons [4]. The unique advantage of soft interfaces is that they have infinite degrees of mechanical freedom [5], which provide users with many perceived affordances. Physical buttons only occupy binary states, and while touchscreens can sense continuous inputs, they require full visual attention from the user, which precludes their use in many common situations where, for example, a user is driving a car [6] or engaged in a virtual reality environment.

Modern touch screens and hand-held controllers primarily use vibration for haptic feedback [7], yet, vibratory amplitude and frequency provide only a limited abstraction of the physical world. Recent advances in microfluidics [8] and soft robotics [9], on the other hand, now supply us with machinery to modulate the shape [10] and compliance [11] of surfaces using rubber with internal fluidic circuits. Additionally, recent work in stretchable electronics has intro-

duced materials that enable soft devices to sense deformation and change their appearance [12]. Conductive leads and electrodes, for example, can be made stretchable though the use of carbon nanotube (CNT) films deposited on elastomeric substrates [13–15]. Similarly, capacitive dielectric elastomer sensors (DESs) have been fabricated using ionic hydrogel conductors as electrodes [16], and more recently stretchable optical fibers have been used as curvature sensors [17]. Yet, despite these advances, we currently lack a modular signal processing framework that can map stretchable sensor signals, which often exhibit noise, hysteresis, and non-stationarity, to application-specific state spaces.

The use of distributed sensor arrays for feedback and control in soft robotics and soft user interfaces requires signal processing that (i) dynamically updates its internal inputoutput mapping to accommodate changes in the system and environment over time, and (ii) has the ability to learn application- and user-specific inputs. Statistical models are well suited for this: they circumvent the need for a physical model of the system, and can learn new inputs without being explicitly programmed. Deep neural networks [18], for example, dominate learning tasks in computer vision [19] and natural language processing [20]. Convolutional neural networks (CNNs), in particular, have many attractive properties for sensory feedback in soft systems including rotation [21], scale [22], and translation invariance, the ability to efficiently extract features from spatially correlated inputs [23], and the ability to perform both classification and regression.

# **OrbTouch Design**

Here we introduce OrbTouch, an inflatable balloon that can recognize arbitrary touch inputs by learning representations of deformations using CNNs. Its touch interface consists of a pressurized silicone orb with an embedded array of CNT-DES's that are capable of high strains ( $\epsilon_{orb} > 100\%$ ). As a user interacts with the interface, the shapes of the capacitors change, inducing a change in their capacitance, which is captured by a data acquisition system. The rubber orb (Fig. 1A; top) changes it shape continuously from circular (i.e., flat; r = 45 mm,  $P_{orb} = 1$  atm) to hemispherical ( $P_{orb} \sim 5.5 \text{ kPa}$ ). The internal components of the device (Fig. 1A; bottom) consist of a single board computer (RBPI3), an analog-digital converter (ADC), and an aircompressor (Fig. 6, Appendix). The air compressor is connected to two push-button solenoid valves that inflate and deflate the orb. The  $5\times5$  sensor array is configured as a passive matrix, with each sensor consisting of a parallel plate

<sup>\*</sup>First author

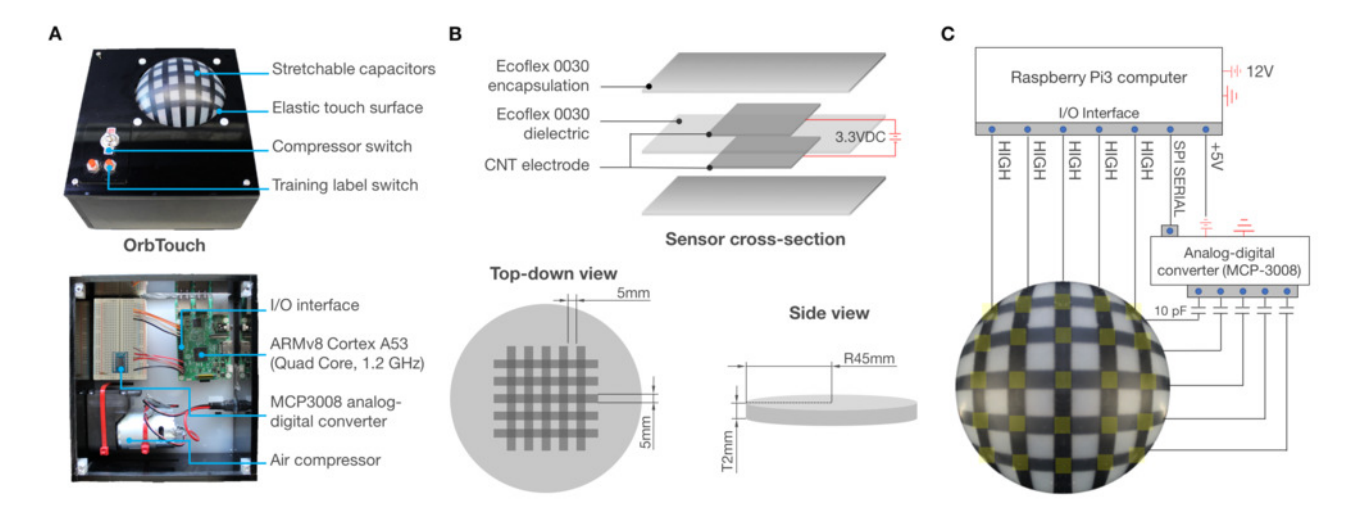


Figure 1: Images and schematic of OrbTouch and its embedded sensor array. (A) Photograph of the OrbTouch device. Its embedded capacitors capture shape changes caused by human touch. The user provides ground-truth labels using a push button located next to the touch surface. Bottom: The embedded RBPI3 computer, ADC, and air compressor used to inflate the orb. (B) Top: a cross-sectional view of the touch interface showing the architecture of our sensors, which consists of upper and lower PDMS encapsulation layers, upper and lower CNT film electrodes, and a 0.5 mm PDMS dielectric layer. Each electrical lead in the passive matrix is  $5 \times 55$  mm, yielding an overall density of 1 sensor cm<sup>-2</sup>. (C) Schematic of the drive electronics used to implement real-time capacitance measurements. To measure capacitance, we set one vertical electrode HIGH (+3.3 VDC) and monitor the induced voltages on the opposite electrodes (i.e., horizontal orientation) using the ADC, which relays the signals to the RBPI3 over SPI serial. During each measurement, there is one pin set HIGH, and one pin that is read; the remaining eight electrodes are connected to ground.

capacitor having two blended MWCNT-SWCNT thin film electrodes that are separated by a PDMS dielectric layer (Fig. 1B; top). The electrodes are deposited by aerosol spraying a dispersion of the CNTs in a solution of 2-propanol and toluene (Appendix) [14]. Electrodes are patterned by placing a stencil on the substrate during deposition. We measure capacitance in the orb using the I/O interface on the RBPI3 and the ADC. To isolate the  $(i,j)^{th}$  capacitor in our array, where  $i,j \in \{0,1,2,3,4\}$ , we charge the  $i^{th}$  electrode to +3.3VDC (vertical orientation, Fig. 1C), and monitor the corresponding voltage rise on the  $j^{th}$  electrode (horizontal orientation, Fig. 1C). We connect each horizontal electrode to a 10 pF capacitor to flip the polarity of the signal prior to feeding it through the ADC, which communicates with the RBPI3 via SPI serial.

# **Deformation-Capacitance Scaling Law**

Information produced in our capacitor array is intimately related to the shape of the membrane. Starting with the principle stretches in the material,  $\lambda_1, \lambda_2, \lambda_3$  (see Fig.2A), we recall that the fractional change in capacitance,  $C/C_0$ , in an incompressible material (where  $\lambda_1\lambda_2\lambda_3=1$ ) is related to its radial stretches via Equation 1.

$$C/C_0 = \lambda_1^2 \lambda_2^2 \tag{1}$$

For an inflating shell the stretch state is approximately equibiaxial tension, where  $\lambda = \lambda_1 = \lambda_2$ , which reduces Equation 1 to  $C/C_0 = \lambda^4$ . There is no known analytic solution relating the radial stretch of an inflated circular shell to its deflection,  $d_{def}$  [24]. Because  $C/C_0$  scales with the square

of the fractional change in the cross-sectional area of the electrodes,  $SA_{ORB}/\pi r^2$ , here we approximate the orb as a hemispheroid and parameterize the stretch by  $d_{def}$ , which we can measure in experiment. Dividing the surface area of the hemispheriodal membrane<sup>1</sup> by the area of the undeformed membrane,  $\pi r^2$ , and taking its square yields the predicted scaling behavior as a function of the radius and deflection (Eq. 2).

$$\frac{C}{C_0} \approx 4 \left( \frac{1}{3} + \frac{2}{3} \left( \frac{d_{def}}{r} \right)^{8/5} \right)^{5/4}$$
 (2)

Figure 2B plots the mean capacitance of our  $5\times5$  CNT-DES grid versus our parameterized function  $\lambda^4(d_{def},r)$  under controlled inflation (tabulated data is provided in Data S1 [25]). The observed behavior undershoots our prediction, which we attribute to the decrease in dielectric permittivity as the capacitor is stretched [16], and to a lesser degree, our approximation of the orb as a hemispheroid [24]. However, the relationship is well defined and monotonic, which enables us to use signals from these capacitors to learn deformations imparted by human touch.

$$SA_{orb} pprox \left[ \frac{r^{16/5} + 2\left(rd_{def}\right)^{8/5}}{3} \right]^{5/8}$$

<sup>&</sup>lt;sup>1</sup>We note that there is no analytic solution relating the surface area of a hemispheroid to its radius and deflection. Here we approximate this relation using the formula given below.

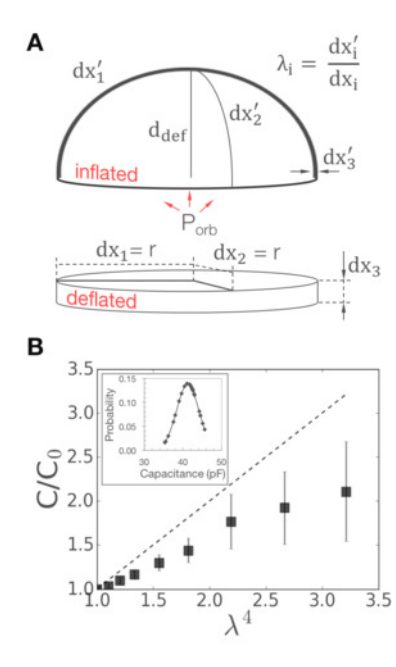


Figure 2: Relationship between deformation and capacitance in the orb. (A) Free body diagram of the touch membrane in the undeformed (deflated) and deformed (inflated) states. Under inflation we assume equibiaxial tension, and thus, because the membrane is incompressible, its stretch state is fully described by the radial stretch. (B) Plot of  $C/C_0$  versus  $\lambda^4$  (n=25). This data is tabulated in Data S1. Inset: The distribution of capacitance values in the undeformed membrane. We observe a mean baseline capacitance of 41.2 pF (SD = 2.9 pF). We note that the capacitive component in our capacitance signal is relatively small (Fig. 7, Appendix).

## **Network Architecture**

OrbTouch captures information from arbitrary touches using convolutional neural networks that learn latent representations of deformation from labeled examples. To demonstrate this, we trained a series of CNNs on a set of touch gestures that we defined for the popular game Tetris. The objective of Tetris is to place a random cascade of falling pieces (Tetrominos) into a bounded rectangle without filling it up; filling a row causes the Tetrominos in that row to disappear, allowing the pieces above it to drop and thus preventing the game board from filling. We control the Tetrominos using the following gestures: finger press (used to translate the Tetromino left, right, and down), rotate CW (used to rotate the Tetromino clockwise), rotate CCW (used to rotate the Tetromino counterclockwise), and pinch (used to drop the Tetromino to bottom). To infer the user's intent and localize their finger presses, we implement two models: (i) an inference network (CNN-G) that maps a queue of 10 5×5 inputs,  ${}^Gz$ , to a categorical probability distribution,  $p_g$ , over five classes of touch gestures  $(\Re^{5\times5\times10} \to \Re^5)$ , and (ii) a regression network (CNN-L) that maps a single input layer,  $^Lz$ , to the x-y location of a finger-press ( $\Re^{5\times5}\to\Re^2$ ). Figure 3A shows a schematic of networks CNN-G and CNN-L, along with an excerpt from the time series used to train

them. Tables 1 and 2 (Appendix) show the input/output shapes, parameter shapes, and nonlinearities used in networks CNN-G and CNN-L, respectively. These models were designed to run on a small CPU (64-bit quad-core, 1.2GHz, 1GB RAM) in real time (10 Hz). Both networks have two hidden convolutional hidden layers and two hidden fully connected layers. The computationally intensive step in these models is the convolutional operation, which is expressed algebraically below in Equation 3,

$$a_{mijk}^{l} = \sigma \left( w_m^l * \mathbf{a}^{'l-1} + \mathbf{b}_m^l \right)_{ijk} \leftarrow \sigma \left( b_m^l + \sum_n \sum_q \sum_r a_{i-n,j-q,k-r}^{'l-1} w_{mnqr}^l \right),$$
(3)

where  $a^l_{mijk}$  is the  $(i,j)^{th}$  node in the  $m^{th}$  feature map in layer l,  $w^l_m$  and  $b^l_m$  are the convolutional kernel and bias terms corresponding to the  $m^{th}$  feature map in layer l, respectively, the operator, \*, denotes the convolution between the kernel and its input, and  $a^{',l-1}$  is the zero-padded input to layer l (we employ same padding). We note that in CNN-L, the time dimension (indexed by k) is singleton. The dense layers following the convolutional layers are mapped by taking the inner product of the weight matrices with the nodes from the preceding layer (Eq. 4).

$$a_{mijk}^{l} = \sigma \left( w_m^{l} * \mathbf{a}^{'l-1} + \mathbf{b}_m^{l} \right)_{ijk}$$
 (4)

# Training

OrbTouch is trained using a label button located next to the touch surface. This button is connected to the I/O interface on the RBPI3 computer; its state is logged at every time step along with the data (sampling rate = 10Hz). To teach OrbTouch gestures, we performed each gesture for  $\sim 5$  min, pressing the label button only when the gesture was being performed ( $n=1.75\times 10^4$ , Data S2 [25]). The network parameters in CNN-G were optimized against the categorical cross-entropy loss with 2-norm regularization applied to its weights (Eq. 5),

$$\ell_{CE}(h(z)) = -\frac{1}{n} \sum_{i=0}^{n} (y \ln(h(z)) + (1 - y) \ln(1 - h(z)))$$

$$+ \lambda_{CE1} \sum_{l=1}^{2} \sum_{m=0}^{M} ||w_m^l||_2^2 + \lambda_{CE2} \sum_{l=2}^{5} ||w^l||_2^2,$$
(5)

where l indexes the layers in the network, and m indexes the feature maps in layer l. We used mini-batches of n=256, and regularization constants  $\lambda_{CE1}=1.875\times 10^{-3}$ ,  $\lambda_{CE2}=5\times 10^{-5}$ . Optimization was implemented using the adaptive momentum estimation algorithm (ADAM) [26]. We performed all training offline on a quad-core CPU using the Tensorflow framework [27]. Figure 3B plots the training and validation accuracy of CNN-G versus training epoch. CNN-G plateaus at a test accuracy of  $\sim 97.5\%$ .

To train network CNN-L, we had a user visually locate each sensor on the membrane and press it (on, off) for  $\sim 30$  min ( $n = 1 \times 10^4$ , Data S3 [25]). Network parameters were optimized against the mean-squared error (MSE, Eq. 6) using ADAM.

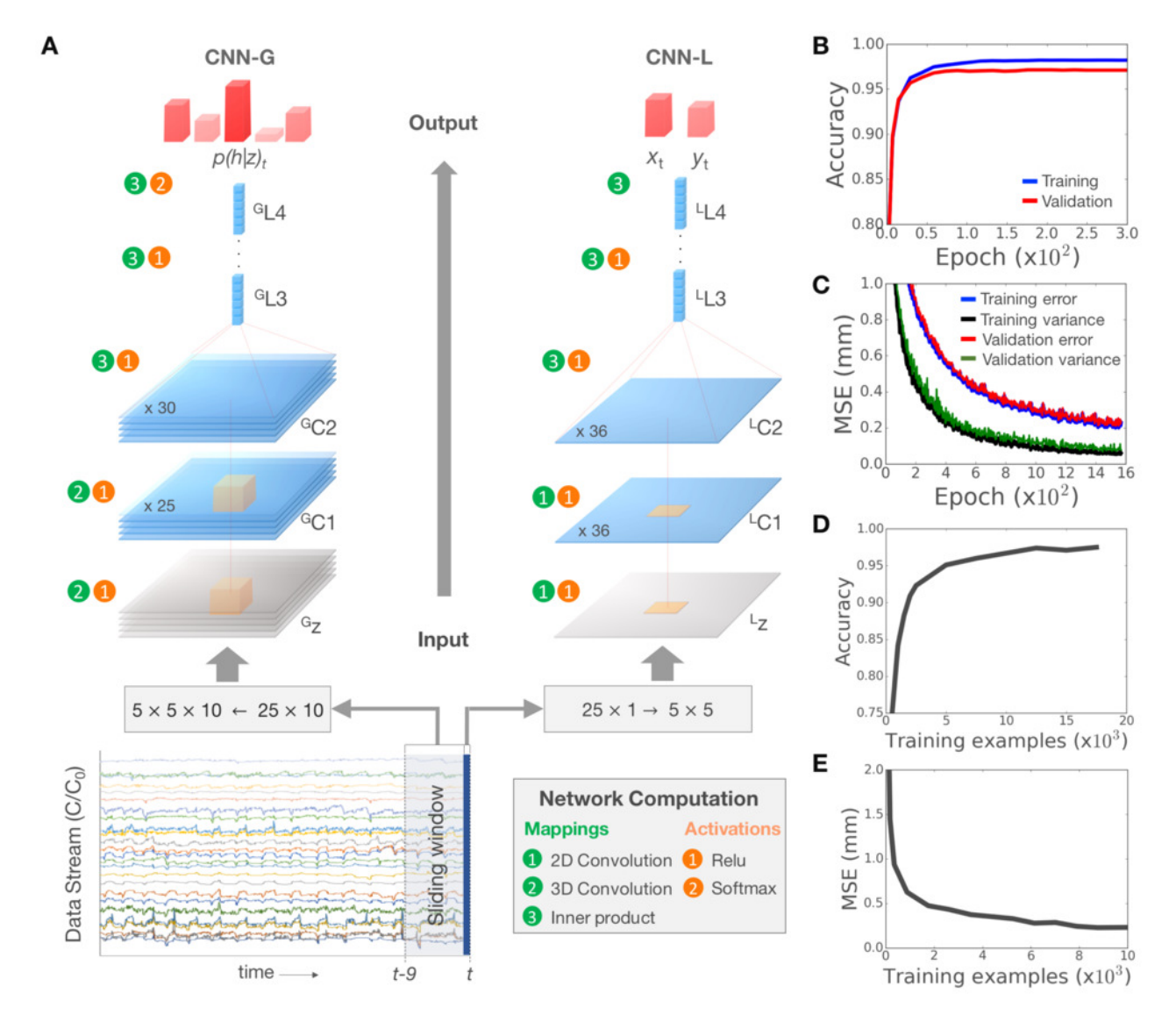


Figure 3: CNN architecture and training results. (A) Schematic of our inference (CNN-G) and regression (CNN-L) networks. Tables 1 and 2 lists the nonlinearities and number of weights and biases used in each layer of CNN-G and CNN-L, respectively. The plot at the bottom shows an excerpt from our 25-channel time series. Network CNN-G accepts as input a sliding window of ten discrete sensor readings  $(5\times5\times10)$  and outputs a probability distribution over five classes (static, finger press, pinch, rotate-CW, and rotate-CCW). Because the information in a gesture is inherently spatiotemporal, we convolve a 3D kernel over both the spatial and temporal dimensions of the input to capture relevant features. Network CNN-L accepts as input a  $5\times5$  sensor matrix and outputs a continuous x-y position. Both networks have two hidden convolutional layers and two hidden fully connected layer. (B) Plot of binary classification accuracy versus training epoch. We measure a test accuracy of 97.5% after  $3\times10^2$  epochs  $(n=1.75\times10^4)$ . (C) Plot of the mean squared error of CNN-L and the variance of its residuals with the training labels, both measured in mm, over  $1.6\times10^3$  epochs  $(n=1\times10^4)$ . (D) Plot of the binary classification accuracy of CNN-G versus number of training examples. (E) Plot of the mean squared error of CNN-L versus number of training examples.

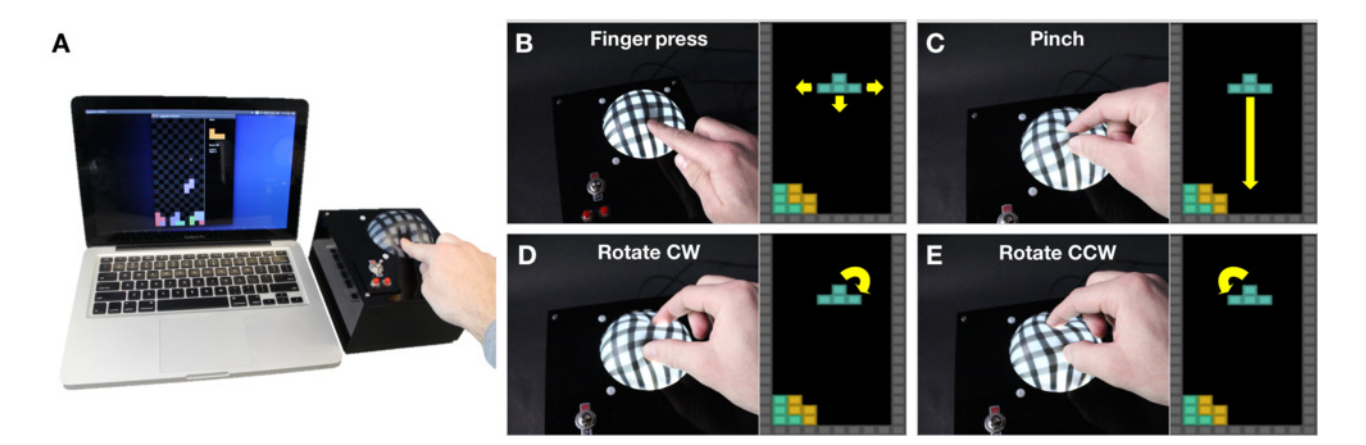


Figure 4: Application of OrbTouch to the popular game Tetris. (A) Photograph of the OrbTouch device being used to control a game of Tetris. We find that four gestures emerge as the dominant modes of interaction among different users. (B) Finger pressing, or poking, is the most common interaction mode—we use it to translate the Tetromino (left, down, right). (C) Pinching is the second most natural interaction mode. Here we use it to drop the Tetromino directly to the bottom of the grid. (D) Clockwise rotation, or twisting, is also very common—here we use it to rotate the Tetromino 90 deg in the clockwise direction. (E) Counterclockwise rotation is used to rotate the Tetromino 90 deg in the counterclockwise direction.

$$\ell_{MSE}(h(z)) = -\frac{1}{n} \sum_{i=0}^{n} (y - h(z))^{2}$$

$$+\lambda_{MSE1} \sum_{l=1}^{2} \sum_{m=0}^{M} ||w_{m}^{l}||_{2}^{2} + \lambda_{MSE2} \sum_{l=2}^{5} ||w^{l}||_{2}^{2}$$

$$(6)$$

We used mini-batches of n=128, and regularization constants  $\lambda_{MSE1}=3\times10^{-4}$ ,  $\lambda_{MSE2}=5\times10^{-5}$ . We added zero-mean Gaussian noise (SD = 0.05 mm) to each ground truth label. Figure 3C plots MSE versus training epoch for CNN-L. We observe a test error of MSE = 0.4 mm and variance var=0.2 mm. For simplicity, we report distances with respect to the undeformed membrane that lies in two-dimensions (i.e., its circular state), where the touch surface spans the x-y interval [(0,0),(4,4)] mm. Thus, for a membrane deflection of  $d_{def}=r$ , a multiplicative factor of  $\pi/2$  provides an approximation of the true error along the curvilinear surface of the orb. Learning curves for CNN-G and CNN-L are shown in Figures 3D and 3E, respectively. Both networks exhibit reasonable performance using only  $\sim 5\times 10^3$  training examples, which is  $\sim 30$  min of total training time.

#### **Using OrbTouch to Play Tetris**

To use OrbTouch as a Tetris controller (Fig. 4A), we wrote a multithreaded program (Fig. 8, Appendix) that collects measurements, implements CNN-G and CNN-L, and communicates with an external host [25]. During gameplay, the user uses OrbTouch to translate (Fig. 4B-C) and rotate (Fig. 4D-E) the Tetrominos as they fall using the gestures that we defined. Our software facilitates this interaction by storing in memory 1 sec of data ( $f=10{\rm Hz}$ ) and passing the relevant inputs to CNN-G and CNN-L. Gestures are inferred by computing  ${\rm argmax}(p_g)$ . In the case of a finger-press, CNN-L is used to determine the location of touch, from which the appropriate translation is generated. These outputs are passed to a debouncing filter that relays commands asynchronously to the host via Bluetooth. Movie 1 [28] shows the real-time output of CNN-G as a user performs a random

sequence of gestures, and movie 2 [29] shows a recording of a Tetris game that uses both CNN-G and CNN-L to generate game commands.

# **Information Theoretic Analysis**

While our Tetris gestures require only  $\sim 2.32$  bits of information, OrbTouch is capable of encoding vocabularies of much higher complexity. As a measure of information content in our system, we compute the Shannon entropy, H(z) (Eq. 7) [30], and mutual information, I(z,y) (Eq. 8), of the capacitance data and labels that were used to train CNN-G (n=34,795),

$$H(z) = \sum_{i=1}^{n} p(z_i) \log_2 \left( p(z_i) \right)$$
 (7)

$$I(z,y) = \sum_{i=1}^{n} \sum_{j=1}^{n} p(z_i, y_j) \log_2 \left( \frac{p(z_i, y_j)}{p(z_i)p(y_j)} \right),$$
(8)

where p(z) and p(z,y) represent the marginal and joint probability masses, respectively. To compute p(z) and p(z,y), we first projected the data and labels onto the interval [0,1] using min-max normalization,  $z \leftarrow (z-z_{min})/(z_{max}-z_{min})$ , for each sensor-gesture combination in the dataset, and then concatenated the data for each sensor into a vector of length 34,795. The data and labels were then discretized into 25-bin histograms.

The complexity of our response variable is straightforward: in the maximum entropy case in which all five gestures occur in equal proportion, the Shannon entropy of  $H(y \sim Unif.)$  is  $\sim 2.32$  bits. We measure a considerably lower value of  $H(y) \sim 1.28$  bits, which is due to the disproportionate number of static labels in the CNN-G dataset  $(p_{g,static} \sim 0.57)$ . For our covariates we compute a mean Shannon entropy of  $H(z) \sim 2.71$  bits (over the 25 sensor channels), which exceeds that required to encode our Tetris labels. With near-optimal encoding, therefore, we could theoretically play Tetris using a single sensor channel as input,

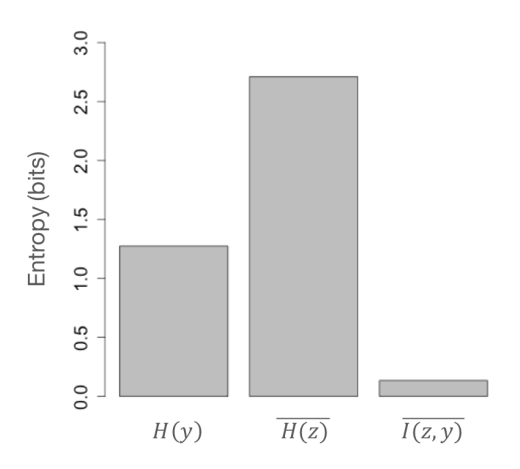


Figure 5: Plot of information entropy statistics computed from the CNN-G dataset. The CNN-G dataset is comprised of 34,795 examples with five categorical labels. The Shannon entropy of a uniformly distributed response variable would be  $H(y \sim Unif.) \sim 2.32$  bits. Here we measure a lower value of  $H(y) \sim 1.28$  bits, which is due to the disproportionate number of static labels in the data  $(p_{g,static} \sim 0.57)$ . We calculate a mean Shannon entropy of  $H(z) \sim 2.71$  bits over our 25 sensors, which is higher than the maximum encoding length that would be required for our Tetris game. These statistics were computed in R using the Entropy package.

and thus with a total of 25 sensors, we expect that OrbTouch is capable of encoding vocabularies of much higher cardinality. We acknowledge that in this case the more relevant statistic is the multivariate Shannon entropy over the entire sensor grid, H(Z), and the mutual information between Z and the response, H(Z,y). Computing these quantities, however, requires the multivariate marginal, p(Z), and joint, p(Z,y), probability masses, which are prohibitively sparse given the size of our training set.

# **Conclusions**

OrbTouch demonstrates the utility of statistical learning algorithms in the rapidly expanding fields of stretchable electronics and soft robotics, and how they can be applied to human computer interaction. Although it was designed with 25 sensors at a density of 1 cm $^{-2}$ , systems of significantly higher density could be afforded through a variety of manufacturing techniques [31, 32]. For example, decreasing the CNT electrode thickness to 500  $\mu \rm m$  using commercially available inkjet printers [32] would yield 100 sensors cm $^{-2}$ . In terms of usability, OrbTouch is intuitive and, although it required  $\sim 1$  hr of training, this time could be decreased significantly using pre-trained networks that have been sensitized to a common set of touch gestures.

While we focus on human computer interfaces, our CNN-based filters are generalizable to other sensing modalities and applications, for example feedback and control in soft robotics. The ability to efficiently extract information from shape lays a foundation for new modes of interaction in virtual reality, wearables, and other HCI and soft robotics applications that use deformable surfaces.

## References

- C. Harrison, S. E. Hudson. Providing dynamically changeable physical buttons on a visual display. Proceedings of the 27th Computer Human Interfaces Conference., 15:299–308, 2009.
- [2] J. Blake, H. B. Gurocak. Haptic glove with mr brakes for virtual reality. *IEEE/ASME Transactions* on *Mechatronics*, 14:606–615, 2009.
- [3] J. G. Elias, W. C. Westerman, M. M. Haggerty. Multitouch gesture dictionary, 2010.
- [4] S. Follmer, D. Leithinger, A. Olwal, A. Hogge, H. Ishii. inform: Dynamic physical affordances and constraints through shape and object actuation. ACM Symposium on User Interface Software and Technology, 13:417–426, 2009.
- [5] D. Rus, M. T. Tolley. Design, fabrication and control of soft robots. *Nature*, 521:467–475, 2015.
- [6] D. Trivedi, C. D. Rahn, W. M. Kier, I. D. Walker. Soft robotics: Biological inspiration, state of the art, and future research. *Applied Bionics and Biomechanics*, 5: 99–117, 2008.
- [7] G. Burnett, G. Lawson, L. Millen, C. Pickering. Designing touchpad iser-interfaces for vehicles: Which tasks are most suitable? *Behavior Information Technology*, 30:403–414, 2011.
- [8] V. Hayward, O. R. Astley, M. Cruz-Hernandez, D. Grant, G. Robles-De-La-Torre. Haptic interfaces and devices. Sensor Review, 24:16–29, 2004.
- [9] G. M. Whitesides. The origins and the future of microfluidics. *Nature*, 442:368–373, 2006.
- [10] R. F. Shepherd, F. Ilievski, W. Choi, S. A. Morin, A. A. Stokes, A. D. Mazzeo, ... G. M. Whitesides. Multigait soft robot. *Proceedings of the National Academy of Sciences*, 108:20400–20403, 2011.
- [11] I. M. Van Meerbeek, B. C. Mac Murray, J. W. Kim, S. S. Robinson, P. X. Zou, M. N. Silberstein, R. F. Shepherd. Morphing metal and elastomer bicontinuous foams for reversible stiffness, shape memory, and self healing soft machines. *Advanced Materials*, 28:2801– 2806, 2016.
- [12] C. Larson, B. Peele, S. Li, S. Robinson, M. Totaro, L. Beccai, ... R. Shepherd. Highly stretchable electroluminescent skin for optical signaling and tactile sensing. *Science*, 351:1071–1074, 2016.
- [13] S. L. Hellstrom, H. W. Lee, Z. Bao. Polymer-assisted direct deposition of uniform carbon nanotube bundle networks for high performance transparent electrodes. ACS Nano, 3:1423–1430, 2009.
- [14] D. J. Lipomi, M. Vosgueritchian, B. C. Tee, S. L. Hell-strom, J. A. Lee, C. H. Fox, Z. Bao. Skin-like pressure and strain sensors based on transparent elastic films of carbon nanotubes. *Nature Nanotechnology*, 6:788–792, 2011.

- [15] O. Kanoun, C. MÃijller, A. Benchirouf, A. Sanli, T. N. Dinh, A. Al-Hamry, A. Bouhamed. Flexible carbon nanotube films for high performance strain sensors. *Sensors*, 14:10042–10071, 2014.
- [16] C. Keplinger, Y. J. Sun, C. C. Foo, P. Rothemund, G. M. Whitesides, Z. Suo. Stretchable, transparent, ionic conductors. *Science*, 341:984–987, 2013.
- [17] H. Zhao, K. OâĂŹBrien, S. Li, R. F. Shepherd. Optoelectronically innervated soft prosthetic hand via stretchable optical waveguides. *Science Robotics*, 1, 2016.
- [18] Y. LeCun, Y. Bengio, G. Hinton. Deep learning. Nature, 521:436–444, 2015.
- [19] A. Krizhevsky, I. Sutskever, G. E. Hinton. Imagenet classification with deep convolutional neural networks. Advances in Neural Information Processing Systems, pages 1097–1105, 2012.
- [20] I. Sutskever, O. Vinyals, O., Q. V. Le. Sequence to sequence learning with neural networks. Advances in Neural Information Processing Systems, pages 3104–3112, 2014.
- [21] S. Dieleman, K. W. Willett, J. Dambre. Rotationinvariant convolutional neural networks for galaxy morphology prediction. *Monthly notices of the royal astro*nomical society, 2:1441–1459, 2015.
- [22] S. Dieleman, K. W. Willett, J. Dambre. Learning hierarchical invariant spatio-temporal features for action recognition with independent subspace analysis. *IEEE Computer Vision and Pattern Recognition*, 2: 3361–3368, 2011.
- [23] Y. LeCun, Y. Bengio. Convolutional networks for images, speech, and time series. The handbook of brain theory and neural networks, 10:3361, 1995.
- [24] J. E. Adkins, R. S. Rivlin. Large elastic deformations of isotropic materials. ix. the deformation of thin shells. Philosophical Transactions of the Royal Society London A: Math, Physics Engineering Sciences, 224:505–531, 1952.
- [25] C. M. Larson. https://github.com/chrislarson1/orbtouch, 2017.
- [26] D. Kingma, J. Ba. Adam: A method for stochastic optimization. arXiv preprint arXiv:1412.6980, 2014.
- [27] M. Abadi, A. Agarwal, P. Barham, E. Brevdo, Z. Chen, C. Citro, ... S. Ghemawat. Tensorflow: Large-scale machine learning on heterogeneous distributed systems. arXiv preprint arXiv:1603.04467, 2016.
- [28] C. M. Larson. https://vimeo.com/213223063, 2017.
- [29] C. M. Larson. https://vimeo.com/213223309, 2017.
- [30] C. E. Shannon. A mathematical theory of communication. Bell System Technical Journal, 27:379–423, 1948.
- [31] M. A. Meitl, Z. T. Zhu, V. Kumar, K. J. Lee, X. Feng, Y. Y. Huang, ... J. A. Rogers. Transfer printing by kinetic control of adhesion to an elastomeric stamp. *Nature Materials*, 5:33–38, 2006.

[32] K. KordÃas, T. Mustonen, G. TÃşth, H. Jantunen, M. Lajunen, C. Soldano, ... P. M. Ajayan. Inkjet printing of electrically conductive patterns of carbon nanotubes. Small, 2:1021–1025, 2006.

# Acknowledgments

We thank K. O'Brien, B. Peele, K. Petersen, and C.W. Larson for their comments, discussions, and insight. This work was supported by the Army Research Office (grant no. W911NF-15-1-0464).

#### **Author Contributions**

C.L. conceived the ideas and experiments detailed in this report; C.L., J.S., R.K., and R.S. contributed to data interpretation and writing. All authors provided feedback.

# **APPENDIX**

# **Device Design & Fabrication**

The internal components of the OrbTouch device consist of a single board computer (Raspberry Pi3; Raspberry Pi Foundation), an analog-digital converter, or ADC (MCP3008; Microchip Corp.), and a 12V DC air-compressor (D2028; AIRPO). Each sensor consists of a parallel plate capacitor with two conductive CNT films separated by a silicone dielectric elastomer layer. Fabrication of the membrane with its embedded sensors is achieved using a multi-step process: (i) in a beaker, a blended mix of MWCNT (P/N 724769; Sigma Aldrich Corp.) and SWCNT (P/N P3-SWNT; Carbon Solutions Inc.) are dispersed in a 90/10 (vol. %) solution of 2-propanol (P/N 278475, Sigma Aldrich Corp.) and toluene (P/N 244511; Sigma Aldrich Corp.) at a concentration of 0.05 wt.% using a centrifugal mixer (SR500, Thinky U.S.A. Inc.) in combination with ultrasonic agitation. (ii) A ~0.5 mm layer of silicone rubber (Ecoflex-0030, Smooth-on Corp.) is cast onto an acrylic sheet and cured. (ii) A layer of tape is overlaid onto the substrate and a laser cutter (Zing 24, Epilog Laser Corp.) is used to selectively remove the tape to form the bottom electrode pattern. (iii) The CNT dispersion is sprayed through the mask with an airbrush (eco-17 Airbrush Master, Master Inc.) to form the bottom electrode. Several coats are applied until the leads reach an end-to-end resistance of  $\sim 1$  kohm. (iv) The mask is then removed and a thin ( $\sim 0.5$  mm) dielectric layer (Ecoflex-0030) is cast over the entire substrate and cured. (v) Steps ii-iv are repeated (in reverse) to form the top half of the membrane (overall thickness  $\sim 2.5$  mm). (vi) External Cu leads are attached to each of the 10 CNT electrodes and connected to I/O pins on the RBPI3 and ADC.

## **Software Design**

Our software was designed to run on a small CPU at 10 Hz. Figure 8 shows a schematic of the program's core functions. The program stores in memory a sliding window of sensor measurements corresponding to data collected over ten time steps (i.e., 1 second of data). Network CNN-G is fed the entire queue, whereas CNN-L looks only at the most recent sensor measurement. The networks are executed in concurrent threads. The network outputs are then fed to a filter that combines them to produce a prediction about

the user's intent. A secondary filter is then used to aggregate these predictions over time, applying a bouncing algorithm to produce commands that are sent to the host via Bluetooth. The rate—limiting step in this program is the computation of CNN-G (because of the 3D convolutional operation), which takes  $\sim\!81\pm9$  ms per forward pass on the RBPI3. We therefore fix the overall latency at 100 ms, and design the other functions of the program to run within this time constraint. This software is implemented in the c++ programming language, and is provided in an external repository [25].

# **Supplemental Movies**

#### Movie 1

Video recording of the real-time output of our CNN-G model [28]. Here we show a person performing each of the five Tetris gestures in a random sequence. OrbTouch uses two convolutional neural networks, CNN-G and CNN-L (Fig. 3A), to perform real-time inference and estimation. These networks were trained on a total of 27,750 examples. Their outputs are passed to two filters: one that produces a prediction pertaining to the intent of the user, and a secondary debouncing algorithm that generates discrete commands. Although we focus on Tetris in this report, our software enables OrbTouch to be reconfigured for any set of arbitrary gestures, allowing it to be used for different applications. The system shown runs at a latency of 100 ms, which could be decreased significantly by parallelizing the neural network computation with a GPU.

#### Movie 2

Video recording of a user playing Tetris with OrbTouch [29]. The game is controlled using finger-presses (Fig. 4B) to translate the Tetromino (left, down, right), pinching (Fig. 4C) to drop the Tetromino directly to the bottom of the board, clockwise twisting (Fig. 4D) to rotate the Tetromino 90 deg in the clockwise direction, and counterclockwise twisting (Fig. 4E) to rotate the Tetromino 90 deg in the counterclockwise direction. The OrbTouch controller runs as a standalone device, and wirelessly communicates with the Tetris application running on the host laptop computer via Bluetooth.

#### **Supplemental Tables**

Table 1: Architecture of neural network CNN-G.

Table 1: Architecture of neural network CNN-G.				
Layer	Shape	Parameters	Activation	
Input $(^{G}z)$	(5, 5, 10)	N/A	N/A	
Conv. L1	(3, 3, 5, 25)	$W_1^G \sim (2, 2, 2, 1, 25)$	Relu	
$(^{G}C1)$		$b_1^G \sim (25, 1)$		
Conv. L2	(2, 2, 3, 30)	$W_2^G \sim (2, 2, 2, 25, 30)$	Relu	
$(^{G}C2)$		$b_2^G \sim (30,1)$		
Dense L3	(720, 1)	$W_3^G \sim (360,720)$	Relu	
$(^{G}L3)$		$b_3^G \sim (720, 1)$		
Dense L4	(720, 1)	$W_4^G \sim (720, 720)$	Relu	
$(^{G}L4)$		$b_4^G \sim (720, 1)$		
Output	(5, 1)	$W_5^G \sim (720, 5)$	Softmax	
(h(z))		$b_5^G \sim (5,1)$		

Table 2: Architecture of neural network CNN-L.				
Layer	Shape	Parameters	Activation	
Input $(^Lz)$	(5, 5)	N/A	N/A	
Conv. L1	(4, 4, 36)	$W_1^L \sim (2, 2, 1, 36)$	Relu	
$(^{L}C1)$		$b_1^L \sim (36,1)$		
Conv. L2	(3, 3, 36)	$W_2^L \sim (2, 2, 36, 36)$	Relu	
$(^LC2)$		$b_2^L \sim (36, 1)$		
Dense L3	(512, 1)	$W_3^L \sim (324, 512)$	Relu	
$(^{L}L3)$		$b_3^L \sim (512, 1)$		
Dense L4	(512, 1)	$W_4^L \sim (512, 2)$	Relu	
$(^{L}L4)$		$b_4^L \sim (512, 1)$		
Output	(2, 1)	$W_5^L \sim (512, 2)$	None	
(x,y)		$b_5^L \sim (2,1)$		

# **Supplemental Figures**

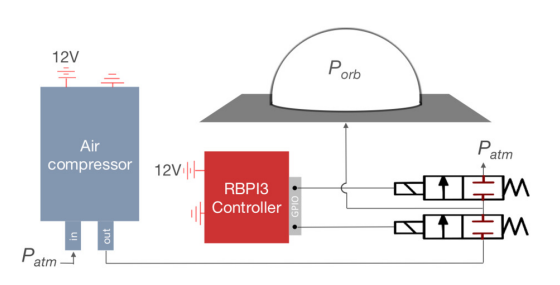


Figure 6: Schematic of the fluidic circuit used to regulate the pressure,  $P_{ORB}$ , inside the OrbTouch device. OrbTouch uses an internal air compressor to inflate its soft touch interface. A push button valve is used to allow pressurized air from the compressor into the orb. The valves are powered by the RBPI3, while the air compressor is powered externally.

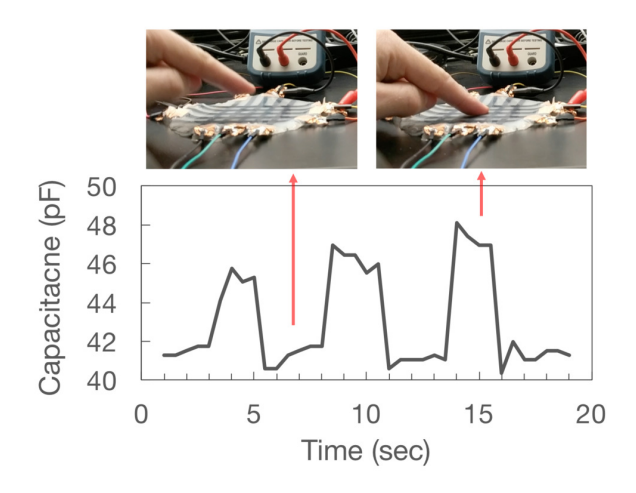


Figure 7: Plot of capacitance versus time as a user lightly touches the undeformed membrane. Here we press the undeformed touch surface at an interval of  $\sim 2.5$  sec (on/off), and observe increases of  $\sim 4.6$  pF ( $\sim 10.9\%$ ) when the surface is touched (with a force similar to what was applied during Tetris; see Movies 1 and 2).

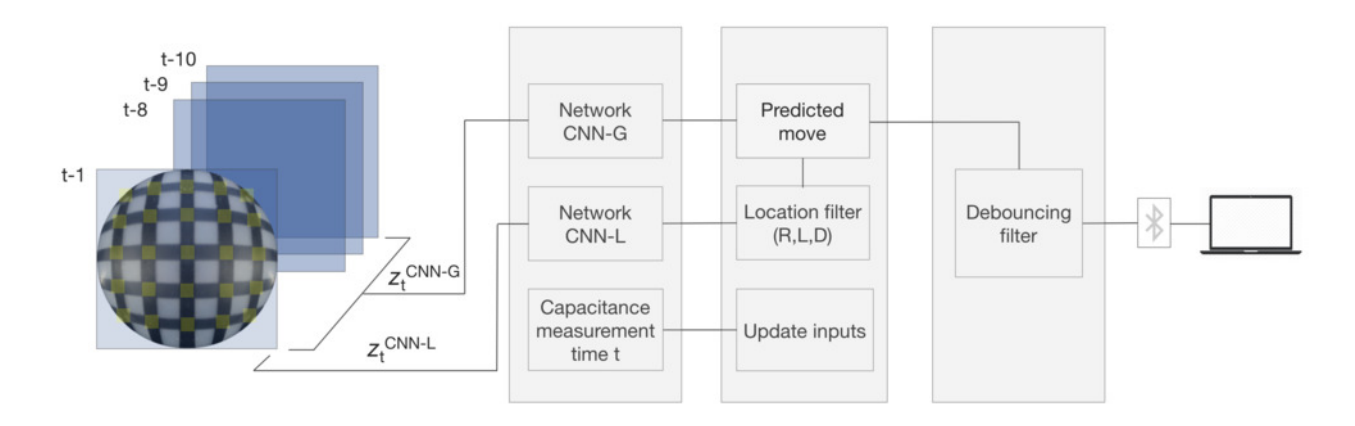


Figure 8: OrbTouch software diagram. The capacitor array is sampled at 10 Hz. The first processing step parallelizes capacitance measurements and the computation of networks CNN-L and CNN-G. The network outputs are then passed to a second processing step that produce a prediction about the player's intent, in parallel with a separate thread that updates the network inputs for the next time step. In the third step, a debouncing filter is used to generate commands, which are sent to a host via Bluetooth. Each cycle of compute take  $\sim 86 \pm 9$  ms—we fix the system latency at 100 ms. This program was implemented in the c++ programming language [25].